Heliyon 10 (2024) e37024

Contents lists available at ScienceDirect

Heliyon

journal homepage: www.cell.com/heliyon

Research article

Fabrication of rGO/BiOI photocathode and its catalytic performance in the degradation of 4-Fluoroaniline

Chenhan Lv [a,b], Haixiang Cheng [a,*], Rui Fan [a], Jingyu Sun [a], Xinghai Liu [b], Yinghui Ji [b]

[a] College of Chemical and Materials Engineering, Quzhou University, Quzhou, 324000, PR China
[b] College of Chemical Engineering, Zhejiang University of Technology, Hangzhou, 310014, PR China

ARTICLE INFO

Keywords:
Photoelectrocatalytic treatment
rGO/BiOI photocathode
4-FA
Decomposition mechanism

ABSTRACT

Organic fluorine compounds are acute carcinogenic and mutagenic to humans. Photoelectrocatalysis (PEC) treatment is an innovative technology in the field of the removal of fluorine compounds, and thus current research focused on improving stability and catalytic ability of photoanode. In this study, it has been synthesized a rGO/BiOI photocathode for the efficient degradation of 4-Fluoroaniline (4-FA). The physical characterization and photoelectrochemical properties of the photocathode was determined. The results indicate that the PEC treatment with the rGO/BiOI photocathode was more efficient compared with individual processes. During the optimization experiments, the PEC treatment achieved 99.58 % and 72.12 % of 4-FA degradation and defluorination within 1 h. Cyclic stability experiments show that rGO/BiOI photocathode was efficient and stable, which reached 96.91 % and 67.64 % of 4-FA degradation and defluorination after five cycles. Mechanism analysis indicates that the PEC process was based on an electrochemical reaction and photo-induced processes. The degradation product of 4-FA was mainly 2,4-di-t-butylphenol, and trapping experiments indicates that h^+ is the primary oxidizing species. Therefore, PEC treatment with rGO/BiOI photocathode is a competitive green approach to remove fluorine compounds pollutants and brings new insights into development of PEC treatment.

1. Introduction

Organic fluorides are widely used in pharmaceutical, printing and dyeing, chemical, military and other fields due to their excellent performance, while leading to ubiquitous presence of fluorides in natural water bodies [1]. Numerous studies reported that excessive fluorides caused severe health issues such as myelosclerosis, osteoporosis, arthritis, tooth mottling, and brain damage [2,3]. 4-Fluoroaniline (4-FA) is a class of chemical compounds with an aromatic ring, a fluorine atom, and an amino group ($-NH_2$). It is both an organic fluorine compound and an aromatic amine compound, thus also exhibiting acute carcinogenic and mutagenic effects [4]. Therefore, industrial wastewater contaminated with fluoride was severely regulated [5], but many countries still have the problems of excessive fluoride levels in drinking water [6]. Therefore, the development of efficient technologies to completely degrade organic fluorides is necessary.

The common processes for treating organic fluorine compounds in wastewater mainly include adsorption method [7], precipitation

* Corresponding author.
E-mail address: chenghaixiang@qzc.edu.cn (H. Cheng).

https://doi.org/10.1016/j.heliyon.2024.e37024
Received 17 March 2024; Received in revised form 26 August 2024; Accepted 26 August 2024
Available online 29 August 2024

method [8], microbiology method [9], and advanced oxidation processes (AOPs) [10]. Physical and microbiology methods have the advantages of simple operation and low cost, but cannot fully achieve the harmless treatment of fluorinated wastewater [11]. AOPs are the promising and competitive green approaches to remove a vast array of organic pollutants, which mainly oxidize refractory organic compounds into low toxicity or even non-toxic small molecule substances by generating strong oxidizing hydroxyl radicals (·OH). However, a single advanced oxidation process technology has limited effect on the organic fluorine compounds removal. Photocatalysis is limited by insufficient quantum efficiency or the possible photodegradation of the catalyst [12]. For example, Maurizio et al. [13] demonstrated fluoride anions would modify the TiO_2 surface, limiting the performances of TiO_2 for degradation. Electrochemical oxidation had the disadvantages of high energy requirements and electrode instability [14]. Therefore, the photoelectrocatalysis process (PEC), which combines the advantages of photocatalysis and electrocatalysis, was often used as a research object for the removal of organic fluorine compounds in wastewater [15]. Its usage has allowed to increase the mineralization efficiency and to reduce the water treatment time [16]. The PEC system has advantages of a small bias voltage, convenience, low energy consumption and high efficiency compared with traditional technologies [17,18]. The development of new light-active materials is essential in PEC system, because a stable and highly efficient photoelectrode provides a consistent supply [19]. Currently, special efforts have been dedicated to the development of anode materials for a PEC system, but continuous application of voltage to the anode in the PEC system can lead to rapid loss of the anode. Hence, the design of cathode on stable and durable materials in the PEC system has been a deserved research. In case of photocathode-PEC system, the reduction reactions could be observed on the semiconductor (photocathode).

An important target of PEC treatment is the development of semiconductor-based photoelectrodes capable of absorbing solar energy and promoting pollutant degradation [20]. The photocatalytic performance of bismuth oxyhalides (BiOX) has gained more and more attention in PEC system because of their special lamellar structure and narrow band gap [21]. Many strategies such as elemental doping [22], heterojunctions constructing [23], morphology control [24] or incorporating cocatalysts [25] were proposed to further enhance the photoelectric conversion efficiency. Among them, the introduction of cocatalysts had been considered as one of the most effective strategies to promote PEC performance for solar energy conversion. The introduction of cocatalyst can suppress recombination of photogenerated charge carriers and further enhance the stability of photoelectrode [26]. Graphene is a 2D-layered structure of sp2-hybridization which possess excellent electrical conductivity and fast transfer pathway to suppress charge recombination and improve the PEC water splitting performance [27]. Huang et al. [28] demonstrated that the decomposition rate constant with SiC/-graphene was 2.2 times higher than that with TiO_2. Kamakshi et al. [29] revealed that the enhancement of degradation efficiency for the introduction of graphene, in which BiOI/rGO enhanced the degradation of MB about 24 % higher than BiOI in 60 min.

In this study, rGO/BiOI photocathode was fabricated by a hydrothermal method and thoroughly characterized. Then, its performance in PEC process on the degradation of 4-FA was investigated. Besides, the catalytic mechanism of rGO/BiOI photocathode was discussed. It can open up a new pathway for the degradation of organic fluorides in PEC.

2. Materials and experimental methods

2.1. Preparation of rGO/BiOI photocatalyst

BiOI was fabricated by a hydrothermal method [30]. First, 2.133 g of Bi $(NO_3)_3 \bullet 5H_2O$ and 0.697 g of KI was dissolved separately in 70 mL of ethylene glycol. Then, the KI solution was added dropwise to the $Bi(NO_3)_3 \bullet 5H_2O$ solution under constant stirring using a magnetic stirrer at room temperature for 30 min. Subsequently, the obtained mixture was taken into a Teflon coated stainless steel autoclave and heated fabricated by a hydrothermal method.

The fabrication of 0.5, 1, 2, and 4 wt % rGO/BiOI nanocomposites were still synthesized by a hydrothermal method. Different mass of graphene oxide (GO) and the as-prepared BiOI nanoparticles were mixed in 50 mL of distilled water. The mixer solution was transferred into autoclave of 200 mL capacity and maintained at 180 °C for 12 h. The product was filtered and washed for 3 times with distilled water to eliminate impurities and then dried at 80 °C to obtain rGO/BiOI after grinding. Analytical grade was used, and all chemicals were purchased from Aladdin Biochemical Technology (Shanghai).

2.2. Preparation of rGO/BiOI photocathode

rGO/BiOI nanocomposites were dispersed in 1 mL of iso-propyl alcohol under the water bath ultrasonication for 30 min. The mixed solution was uniformly spread onto the graphite substrate to form a film with an area of 5 cm × 5 cm, and then dried at 80 °C for 30 min. The as-treated graphite substrate was soaked in deionized water and dried in an oven at 80 °C, thus obtaining the rGO/BiOI photocathode. Analytical grade was used, and all chemicals were purchased from Aladdin Biochemical Technology (Shanghai). The graphite substrates were purchased from King Carbon Technology (Beijing).

2.3. Characterization

The morphologies and microstructures of the rGO/BiOI nanocomposites were investigated by a scanning electron microscope (SEM, SU8010, Hitachi, Japan). The crystal structure was analyzed using X-ray diffraction (XRD, Burker D8 Advance, Germany) with Cu K_α in the 2θ range of 10°–60°. Fourier transform infrared (FTIR) spectroscopy was obtained using the FTIR spectrometer model TENSOR27 with a scan range 400–4000 cm^{-1}. The structural and chemical properties of nanocomposites were investigated by a Raman spectrometer (Raman, Lab RAM HR Evolution, Horiba, Japan) with a scan range 0–1350 eV. The elemental chemical

composition was further detected by using X-ray photoelectron spectroscopy (XPS, ESCALAB Xi$^+$, Thermo Fischer, USA), using Al K_α ($h\nu$ = 1486.6 eV) as irradiation source. Diffuse reflectance spectra were recorded using a UV–Visible spectrophotometer (Lambda 650S, PerkinElmer, USA). $BaSO_4$ was used as blank reference during the test, and the spectral range was 200–800 nm. The electrochemical workstation (CHI760E, Shanghai Chenhua, China) was used for the cyclic voltammetry (CV) measurement. Electrochemical impedance spectroscopy (EIS) test and electrochemical characterizations were performed under xenon lamp irradiation. The rGO/BiOI photocathode served as the working electrode, the reference electrode was a saturated calomel electrode, and the Ti/IrO_2 electrode was a counter electrode.

2.4. PEC experiments

The rGO/BiOI-PEC process was performed in a cylindrical reactor with a reaction volume of 1 L containing 100 mg/L of 4-FA (Fig. 1). The Ti/IrO_2 anode (5 cm × 5 cm, purchased from Shanghai Yiming) and rGO/BiOI photocathode (5 cm × 5 cm) with a spacing of 5 cm were used, respectively. Previous works disclosed that the sunlight simulated by the xenon lamp has over 98 % optical overlap with real sunlight [31], thus a xenon lamp was used for simulating sunlight generated for the photocatalytic reactions. The bias voltage was provided by a digital DC regulated power supply (UTP1306S).

The removal efficiency of 4-FA in the rGO/BiOI-PEC process was tested as a function of rGO mass percentage (values of 0.5, 1, 2, and 4 wt %), NaCl concentration (values of 1, 3, 6, and 12 g/L), current intensity (value of 0.5, 7.5, 1.25, and 1.75 A), illumination strength (values of 10, 15, and 20 A), solution pH (values of 3, 7, and 10). The whole reaction solution was continuously stirred on a booster electric stirrer at 25 ± 1 °C. Analytical grade was used, and all chemicals were purchased from Aladdin Biochemical Technology (Shanghai).

2.5. Analytical methods

The experiments were carried out for 1 h to evaluate the activity of the as-prepared rGO/BiOI photocathode. At predetermined intervals (10 min), 2 mL of the reaction solution was withdrawn and filtered through 0.22-μm needle filter. The 4-FA concentration in the filtrate was measured by a spectrophotometric method (Water quality-Determination of aniline compounds-Spectrophotometric method with N- (1-naphthyl) ethylenediamine). The removal efficiency (%) was calculated by comparing the 4-FA concentration at the start of reaction and that at time t (Fig. S1). The kinetic constants were determined using the analyzed concentrations of 4-FA by a pseudo-first-order kinetic model, as shown in Eq. (1):

$$\frac{dC}{dt} = -K_1 C \tag{1}$$

where, C denotes the concentration of 4-FA (mg/L), t denotes time (min), and K_1 denotes the kinetic constant (min^{-1}) [32].

The fluoride concentration in the filtrate was examined by fluoride ion-selective electrode method (Fig. S2). The defluorination efficiency (Y%) calculated as Eq. (2).

$$Y\% = 100\% \times m(F^-) / 18.998 \times C_0 / 111.12 \tag{2}$$

where, $m(F^-)$ is the detected fluoride ion concentration (mg/L), C_0 is the initial 4-FA concentration (mg/L).

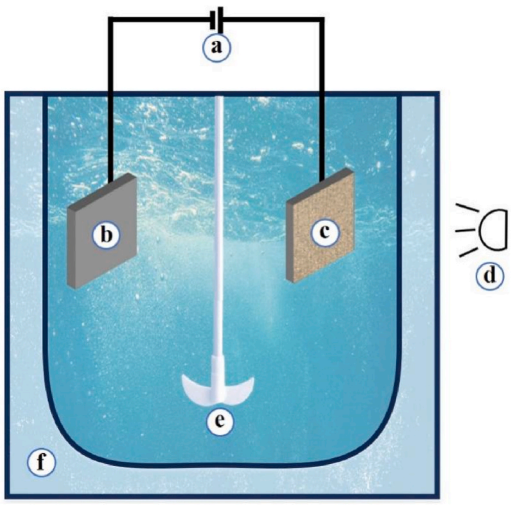

Fig. 1. Schematic diagram of the experimental setup (a: power supply; b: Ti/IrO_2 anode; c: rGO/BiOI photocathode; d: xenon lamp, e: stirring paddle, f: coolant layer.).

In addition, the samples were collected at specified intervals, filtered through a 0.45-μm PTFE (polytetrafluoroethylene filter cartridge) filter and then analyzed by gas chromatography-mass spectrometry (GC-MS, QP2020NX, SHIMADZU, Japan). GC conditions: The temperature of the injector was 250 °C, and the flow rate was 1.0 mL/min, The column temperature was initially 80 °C and held for 3 min, then increased to 180 °C at a rate of 15 °C/min, and finally increased to 280 °C at a rate of 5 °C/min and held for 5 min. MS conditions: The ion source was EI (electron ionization), and the mass scanning range was 30–1000 *m/z*.

3. Results and discussions

3.1. Characterization

3.1.1. SEM analysis

The surface morphological characteristics of BiOI and rGO/BiOI were investigated by SEM (Fig. 2a−2d). It can be seen that a clear flower-like BiOI microspheres approximately 8 μm (Fig. 2a). Upon magnification, the spherical crystals were formed by aggregation of many sheets like nanoplates (Fig. 2b). A wrinkled and flaky structure can be clearly observed on the surface of the spherical structure, and the flaky nanosheets of BiOI became more looser (Fig. 2c and d).

3.1.2. XRD analysis

Fig. 3 shows the XRD patterns of BiOI and rGO/BiOI. In the XRD pattern of BiOI, the highest diffraction peaks are observed at 29.13°, 31.76°, 37.42°, 45.49°, 49.67°, 55.06°, 60.02° and 66.23° with corresponding planes as (102), (110), (112), (200), (005), (212), (213) and (220) of BiOI (JCPDS 10–0445), respectively [33]. The highest noticeable peak of BiOI is (102) and (110) indicating that BiOI was a tetragonal phase and well crystallized. A quite low diffraction peak at 24.2° from rGO was detected in composite, which is due to the lower loading and generally weaker diffraction intensity of rGO [34]. It also indicates that the complete dispersion of rGO was achieved during catalysts preparation [35]. In addition, sharp characteristic absorption peaks in the BiOI spectrum also appear at corresponding positions in the rGO/BiOI spectrum, indicating that there was no change in the BiOI crystal structure of nanocomposite.

3.1.3. FTIR and Raman analysis

Fig. 4a shows the results of the FTIR analysis of GO and rGO/BiOI. In the rGO/BiOI spectrum, the band at 500 cm^{-1} is the stretching vibration of Bi-O indicating the preparation of BiOI. In the GO spectrum, the bands located in 1016 and 1264 cm^{-1} are a result of stretching vibrations of C-OH, the bands around 1392 and 1627 cm^{-1} are the stretching vibration of C-O (alkoxy and epoxy groups) and C=C bonds, respectively. Furthermore, the band around 3446 cm^{-1} is attributed to the bending (δ(O-H)) and stretching (ν(O-H)) frequencies of the hydroxyl group [36]. Corresponding absorption peaks are also observed at similar positions in the rGO/BiOI spectrum, indicating that BiOI was successfully adhered to the graphene oxide layer. In addition, compared with the spectrum of GO, the absorption peak of oxygen-containing functional groups in rGO/BiOI decreases, which confirmed formation of reduced graphene oxide [37].

Then, Raman spectra was further used to deeply analyze the chemical structure [38]. Two bands are observed at 80.27 cm^{-1} and 150.50 cm^{-1}, which are ascribed to the A_{1g} and E_g stretching vibration of the Bi-I bond (Fig. 4b). The two Raman peaks are also observed in the Raman spectrum of rGO/BiOI in Fig. 4c, and their peak positions, intensities, and peak shapes are relatively similar.

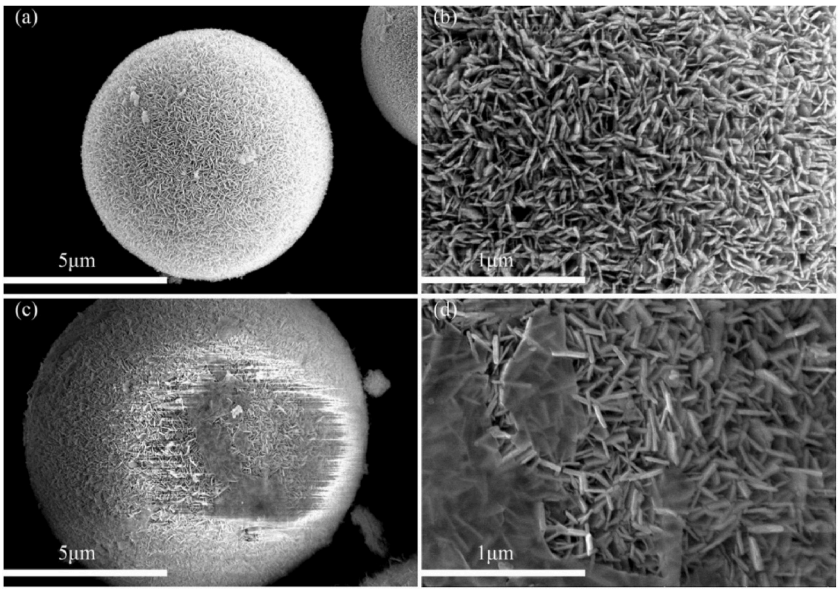

Fig. 2. SEM images of the rGO (a, b) and rGO/BiOI (c, d).

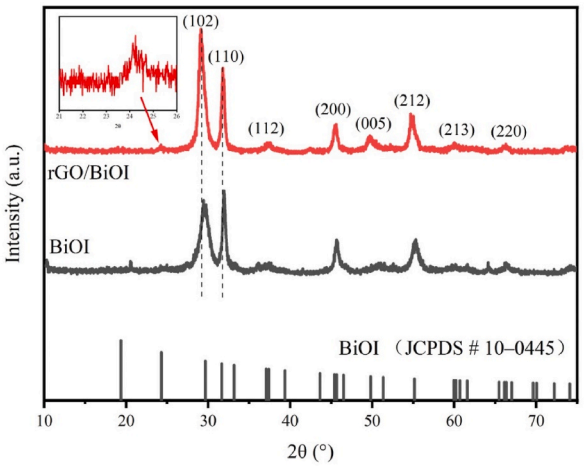

Fig. 3. XRD patterns of BiOI and rGO/BiOI nanocomposite.

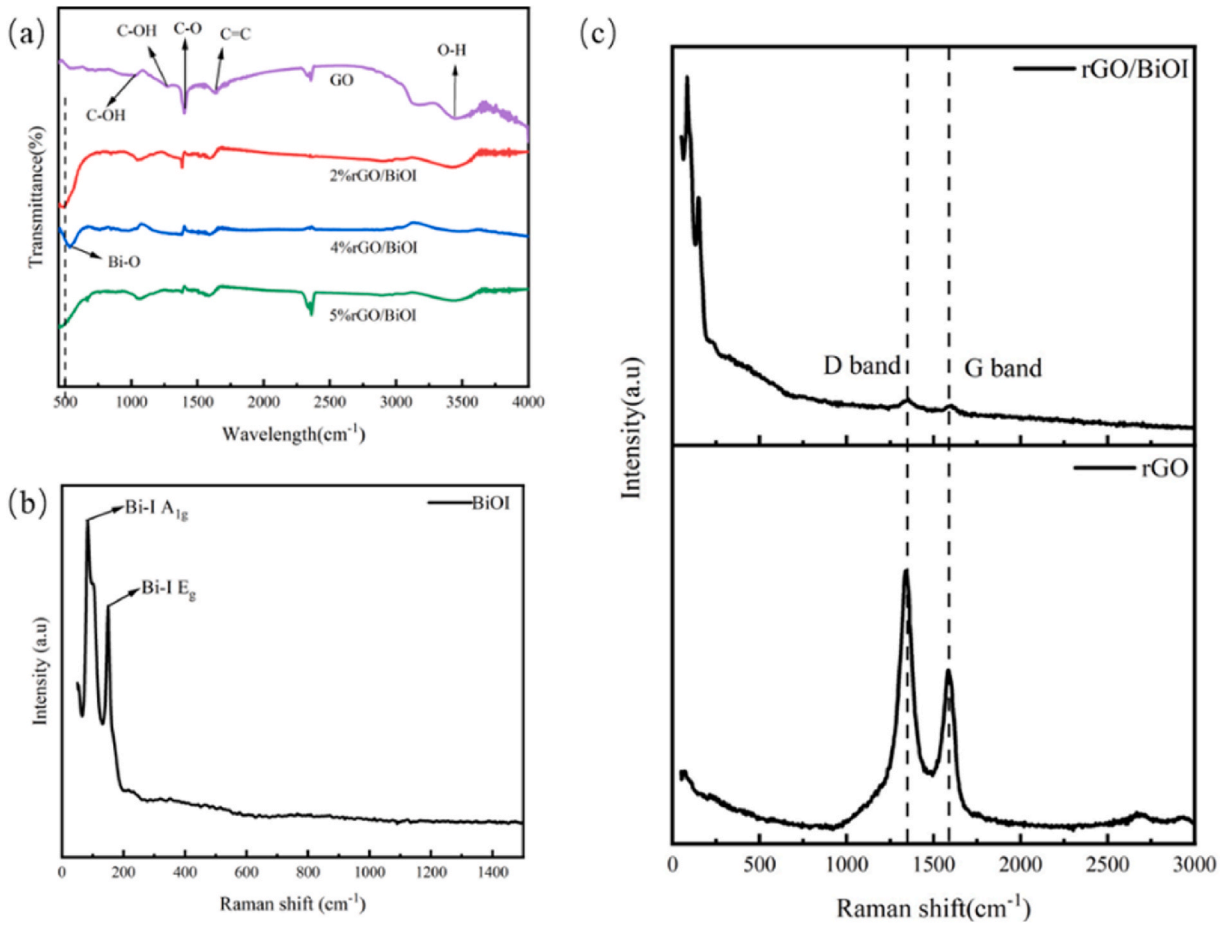

Fig. 4. (a) FT-IR spectra. (b) Raman spectra of BiOI. (c) Raman spectra of rGO/BiOI and rGO.

The results indicate that the material composite did not change the BiOI structure, which is consistent with the results of XRD. In addition, two characteristic peaks of graphene at 1348 cm^{-1} and 1590 cm^{-1} are observed in both rGO and rGO/BiOI samples, which confirms the presence of rGO in composites (Fig. 4c). These two peaks are attributed to the amorphous disordered carbon (D-band) and graphitic carbon (G-band), respectively [39]. The ratio of I_D/I_G are 1.57 and 1.97 for rGO and rGO/BiOI, respectively. The higher I_D/I_G

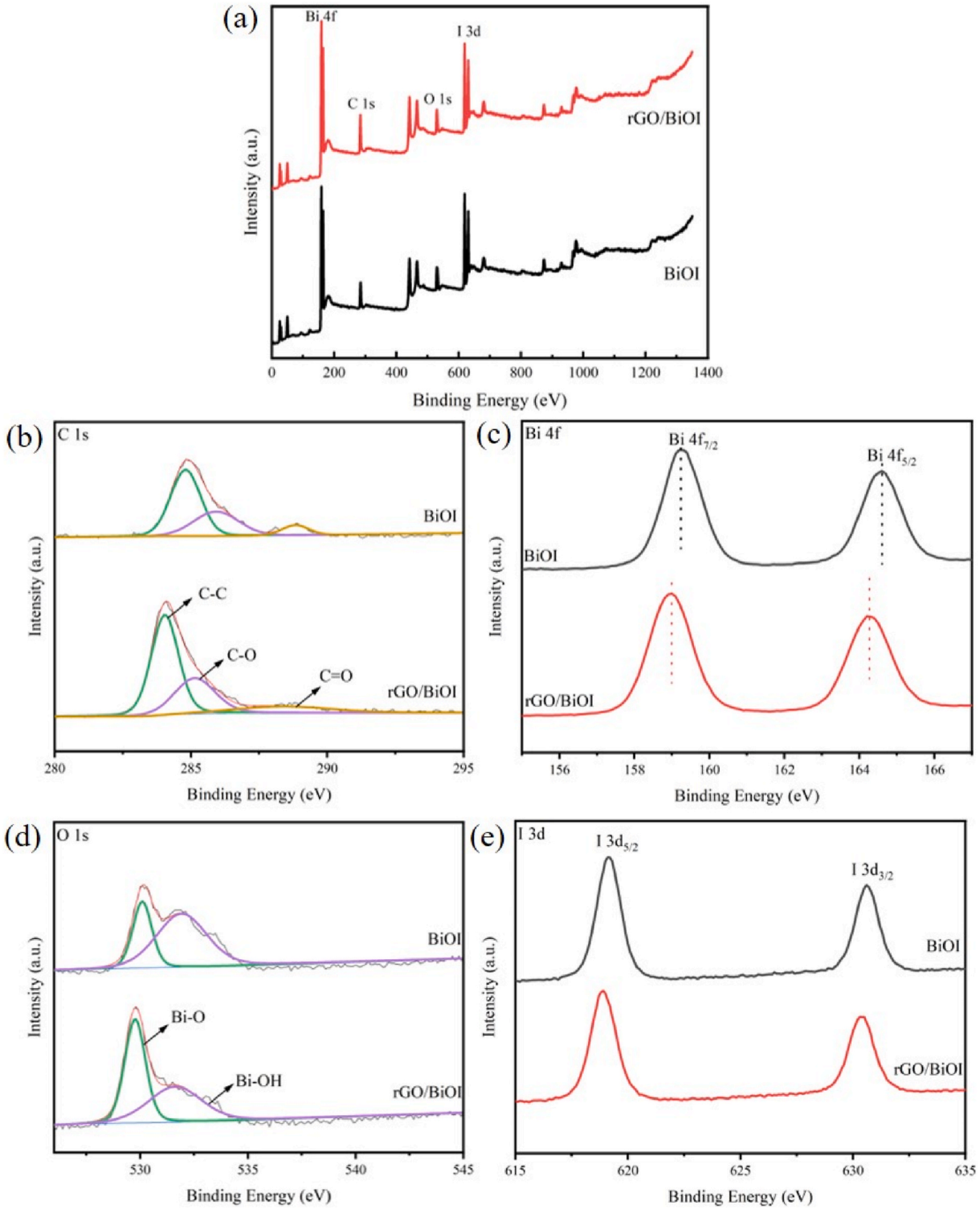

Fig. 5. (a) XPS survey spectra of BiOI and rGO/BiOI. (b) XPS C 1s spectra. (c) XPS Bi 4f spectra. (d) XPS O 1s spectra. (e) XPS I 3d spectra.

value signifies the charge transfer between rGO and BiOI, and implies a higher defect domain and active surface area in the hybrid [40].

3.1.4. XPS measurements

The XPS survey spectra (Fig. 5a) shows that the rGO/BiOI nanocomposites contained Bi, I, O and C elements. To further investigate the chemical bonds between various elements, peak fitting was performed by software. The peaks of C 1s at 284.73, 285.92 and 288.83 eV are attributed to C-C, C-O, and C=O bonds (Fig. 5b). In Fig. 5c, two distinctive peaks at 159.3 and 164.6 eV are assigned to Bi $4f_{7/2}$ and Bi $4f_{5/2}$, respectively, confirming the presence of Bi^{3+} [41]. The peaks at 530.0 and 531.3 eV correspond to Bi-O and Bi-OH, respectively (Fig. 5d). The $3d_{5/2}$ and $3d_{3/2}$ of I^{-} are located at 619.1 and 630.5 eV, respectively (Fig. 5e) [42]. In addition, the peaks of Bi $4f_{7/2}$ and Bi $4f_{5/2}$ in rGO/BiOI shift up by 0.3 and 0.3 eV compared with BiOI. The peaks of Bi-O and Bi-OH in rGO/BiOI also shift by 0.4 and 0.3 eV compared with BiOI. All the chemical shifts indicate that chemical interaction was formed between rGO and BiOI [43,44]. The results confirm the presence of BiOI and rGO in the prepared samples, which are in concurrence with the XRD.

3.1.5. UV–vis spectroscopy

As shown in Fig. 6a, pure BiOI has an excellent visible light absorbance, and the absorption edge of BiOI is about 650 nm. Then, the absorption edge of the samples shows the red shifts with rGO loading. The remarkable shifts in absorption value enhanced the photocatalytic efficiency in the visible region, and the 4 % rGO/BiOI shows the highest absorption intensity in the visible light range. The bandgap energy values (Eg) of photocatalysts are estimated using the empirical formula (Eq. (3)) with Tauc method.

$$\alpha = \frac{A(h\upsilon - Eg)^{n}}{h\upsilon} \tag{3}$$

where, α is the absorption coefficient, A is the proportionality constant, h is the Planck constant, υ is the frequency, and n is 2 for the indirect transition of a semiconductor [45]. The x-axis intersection point of the linear fit of Tauc plot gives the band gap energy. Fig. 6b illustrates that rGO/BiOI has lower band gap energy (1.44 eV) than BiOI (1.66 eV). Therefore, lower excitation energy is necessary to produce electron transition in rGO/BiOI, enhancing the photocatalytic activity. Such a phenomenon can be explained by the formation of a hybridized structure between rGO and BiOI, which effectively stimulated the migration efficiency of photo-induced charges and suppressed the charge recombination [46].

3.1.6. Electrochemical analysis

The CV curves of BiOI photocathode and rGO/BiOI photocathode are showed in Fig. 7a. The BiOI photocathode and rGO/BiOI photocathode have prominent reduction peaks at 0.23 and 0.41 V, respectively. Obviously, the rGO/BiOI photocathode shows more substantial reduction peaks than BiOI photocathode, increasing by 0.73 mA/cm^{-2}. It may be attributed to graphene enhanced the charge transfer process. The specific capacitance of photocathode was calculated by Eq. (4), [47].

$$C_p = \frac{1}{m\nu(V_f - V_i)} \int_{V_i}^{V_f} i(V)\, dV \tag{4}$$

where, C_p is the specific capacitance (F/g), m is the mass of active material (g), (V_f-V_i) is the applied potential window (V), ν is the scan rate (V/s), and the integral term represents the area under the CV curve calculating from CV data using Origin Lab software. The CV curve areas of rGO/BiOI photocathode is 0.8 larger than that of BiOI photocathode, which means a higher specific capacitance [48]. It indicate that the rGO/BiOI photocathode had more electrochemically active sites and exhibited a more outstanding PEC performance.

The interfacial charge transfer resistance (Rct) of BiOI and rGO/BiOI photocathode is show by the Nyquist plot of EIS spectra

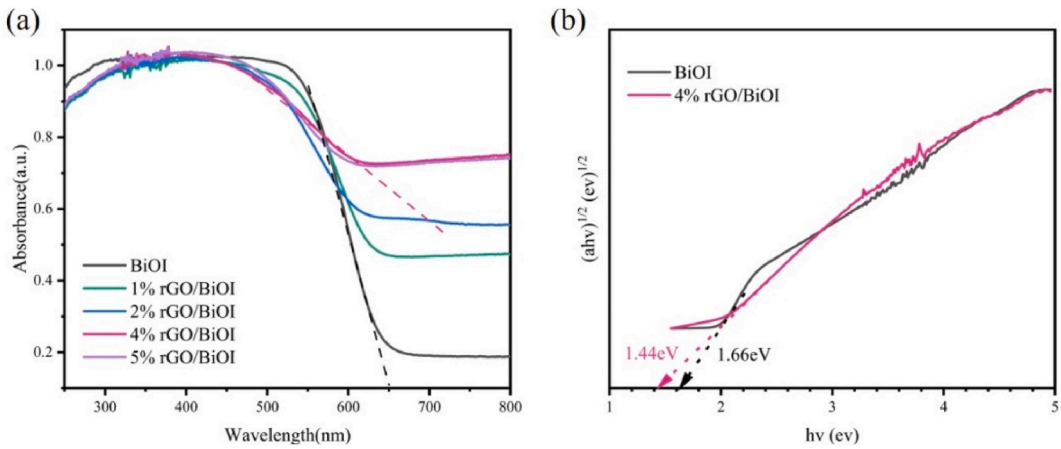

Fig. 6. (a) UV–vis diffusion reflectance spectra of rGO/BiOI at different mass percentage. (b) the band-gap spectra of BiOI and rGO/BiOI.

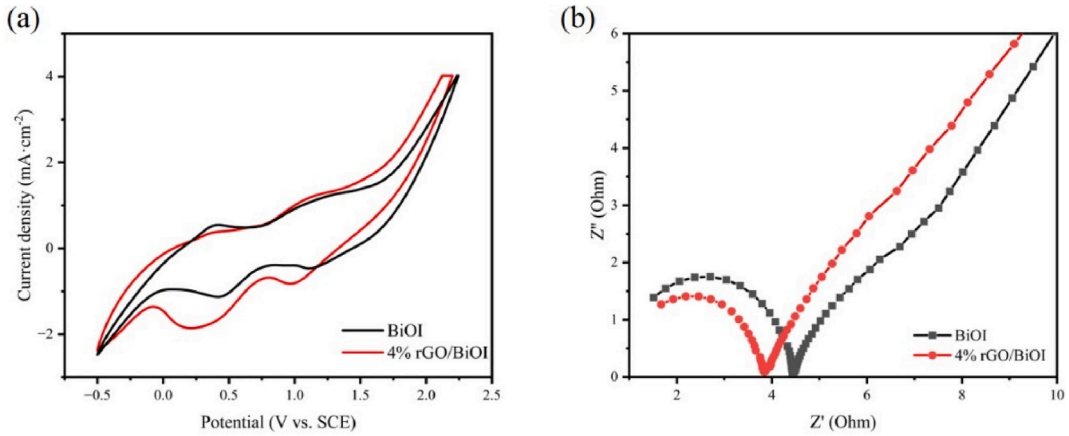

Fig. 7. Electrochemical analysis of rGO/BiOI photocathode: (a) CV. (b) EIS.

(Fig. 7b). The smaller the semicircle diameter of the Nyquist plot, the smaller the *R*ct of the photocathode and the higher the electron transferability [49], which is more advantageous for photoinduced charge carrier transfer and separation. Hence, the rGO/BiOI photocathode has smaller *R*ct and stronger electron transferability, indicating that rGO on the photocathode could improve the efficiency of pollutant removal. The findings are in accordance with the results of CV curves in Fig. 7a.

3.1.7. Photoelectrocatalytic experiments

The photo-electrocatalytic activity of the photocathode was tested by the degradation rate and defluorination efficiency of 4-FA. Comparing with different rGO mass percentages, 4 % rGO/BiOI graphite cathode shows the highest degradation and defluorination rates, reaching 72.36 % and 40.78 % in 10 min, respectively (Fig. 8). Additionally, the degradation rates of 4-FA by 4 % rGO/BiOI were 2.03 and 1.80 times than graphite cathode and BiOI graphite cathode, respectively. The defluorination efficiencies of 4-FA by 4 % rGO/BiOI are 2.87 and 2.22 times than graphite cathode and BiOI graphite cathode, respectively. The 4-FA decomposition kinetics are fitted by the pseudo-first-order model (Table 1). Obviously, the rate constant of 4 % rGO/BiOI was the highest, with a value of 0.0759 min^{-1} (R^2, 0.962). The 4 % rGO/BiOI exhibited the highest photo-electrocatalytic performance in the degradation and defluorination of 4-FA, which is consistent with the results of UV–Vis (Fig. 6). Compared with individual photocatalysis and electrocatalysis (Fig. S3), PEC process has higher performance (80.70 % and 40.58 % of 4-FA degradation and defluorination after 4 h in photocatalysis, and 97.49 % and 64.16 % of 4-FA degradation and defluorination rates after 1 h in electrocatalysis).

3.2. Photoelectrocatalytic experimental results

3.2.1. Effect of NaCl concentration

Electrolytes are extremely important factors that increase the conductivity of a solution and guarantee excellent ion transfer in the PEC systems [50]. Therefore, in this study, different concentrations of NaCl were used to determine whether electrolyte greatly affected the degradation of the 4-FA. The rate constants at 1, 3, 6, 12 g/L of Cl^- were 0.02818 min^{-1} (R^2, 0.993), 0.06096 (R^2, 0.978),

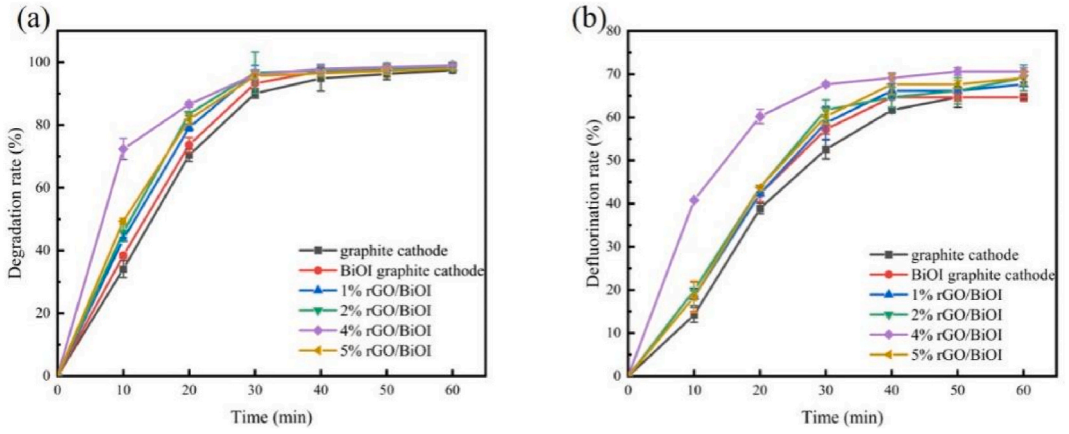

Fig. 8. The different rGO/BiOI photocathodes degradation performance (Conditions: NaCl concentration of 6 g/L, current intensity of 0.75A, illumination strength of 15A, pH of 7). (a: degradation rate; b: defluorination efficiency).

Table 1
Photo-electrocatalytic decomposition of 4-FA by the different photocathodes and the corresponding kinetic rate constants.

Photocathode Material	4-FA Degradation Rate (%)	defluorination efficiency (%)	Pseudo-First-Order Rate Constant (min^{-1})	Regression coefficient (R^2)
Graphite	97.94	64.65	0.0655	0.967
BiOI Graphite	97.97	64.66	0.0741	0.939
1 % rGO/BiOI	98.12	67.64	0.0742	0.934
2 % rGO/BiOI	98.84	69.13	0.0757	0.966
4 % rGO/BiOI	98.94	70.63	0.0759	0.962
5 % rGO/BiOI	98.00	69.13	0.0685	0.919

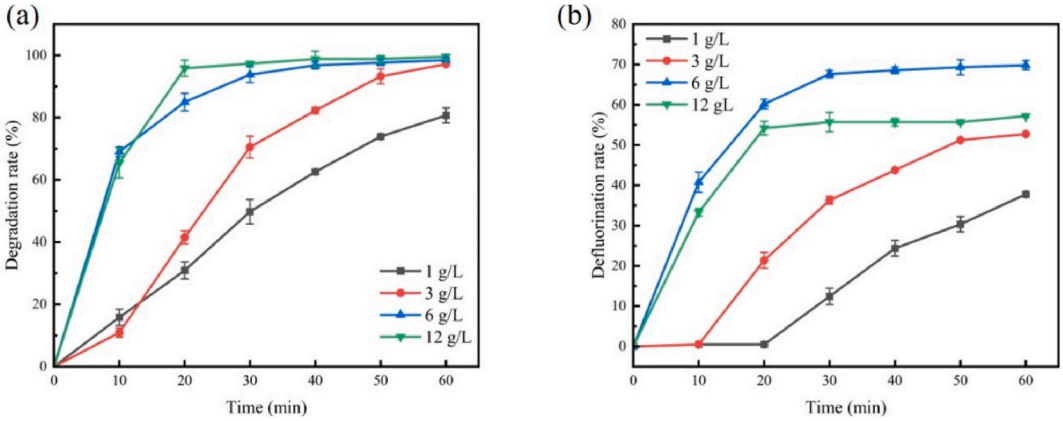

Fig. 9. 4-FA degradation (a) and defluorination (b) under different NaCl concentration.

0.07595 (R^2, 0.981), 0.08674 (R^2, 0.957), respectively (Table S1). Accordingly, both degradation rate and defluorination efficiency of 4-FA increased with an increasing concentrations of Cl^- (Fig. 9). The above Cl^- concentration had positive effect on the decomposition of 4-FA. However, the removal efficiency of F^- was decreased from 57.20 % to 49.74 % as the Cl^- concentration ascended from 6 to 12 g/L. In general, the excess of Cl^- competed for radicals with the pollutant [51].

3.2.2. Effect of current intensity

The effect of current intensity on the decomposition of 4-FA is shown in Fig. 10. The degradation efficiency of 4-FA increased with the increase of current intensity from 0.5 to 1.25 A, and 99.58 % of 4-FA degradation efficiency was determined at 1.25 A. A further increase of current intensity above 1.25 A led to a slight decrease in the defluorination efficiency, which is consistent with the change in rate constants (Table S1). Furthermore, the defluorination rate first increased and then decreased with the increase of current intensity, and 70.63 % of 4-FA degradation efficiency was highest at 0.75 A. The decrease in degradation and defluorination efficiency at higher current intensity can be attributed to the oxygen evolution reaction (OER) and hydrogen evolution reaction (HER). The rates of

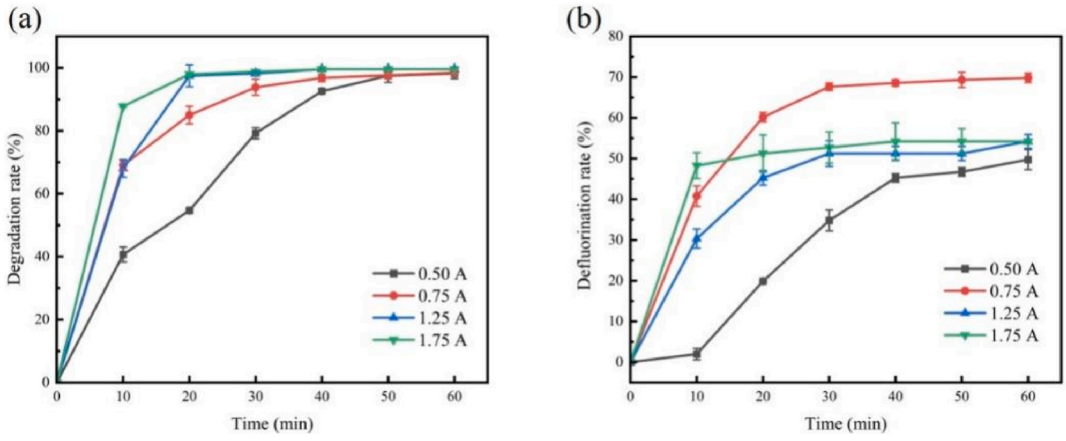

Fig. 10. 4-FA degradation (a) and defluorination (b) under different current intensity.

ORE and HER will rapidly improve with the increase of current intensity, which caused a serious competition between the OER and the reaction of decomposition of 4-FA [52].

3.2.3. Effect of illumination strength

From Fig. 11, it could be observed that the degradation efficiency of 4-FA has little changes and the defluorination rate has an improvement in an increase of illumination strength. (这一段是否考虑放到SI里?)

3.2.4. Effect of pH

pH is the one of key factors affecting the degradation and elimination of pollutants, and can considerably affect the performance of PEC process by influencing the distribution of electric charge on the nanocomposite surface. Fig. 12 shows that the degradation and defluorination efficiency reached a maximum value (98.94 % and 70.63 %) at a neutral pH, therefore, the PEC process could degrade pollutant without any pH adjustment.

3.4. Mechanism of decomposition

.

3.3. Recycling of rGO/BiOI photocathode

The stability of rGO/BiOI photocathode was investigated to confirm the stability of the material during the photocatalytic activity. The same photocathode was cleaned and dried after first reaction, and then used for the next cycle (2−5 cycles). The data shows that the degradation and defluorination percentage of 4-FA in PEC systems were 96.91 % and 67.64 after five cycles, respectively, with only a slight loss (Fig. 13). It proves an excellent stability and robustness of the BiOI/rGO photocathode potential for long-term applications.

3.4.1. Reactive species

In order to investigate the roles of reactive species responsible for the degradation and defluorination of 4-FA with rGO/BiOI photocathode, the trapping experiments were carried out and the obtained results were shown in Fig. 14. For these experiments, EDTA-2Na (to trap h^+), isopropanol (IPA, to trap ·OH) [53], *p*-benzoquinone (*p*-BQ, to trap $\cdot O_2^-$) [54] and tert-butanol (TBA, to trap ·OH and Cl^-) [55] were used as scavengers (0.1 M).

The photoelectrocatalytic degradation and defluorination percentage decreased by 11.14 % and 32.83 % when EDTA-2Na is added, indicating that h^+ played a vital role in 4-FA decomposition by rGO/BiOI photocathode. After adding IPA, the 4-FA degradation and defluorination rate decreased by 3.07 % and 19.40 %, which implies that ·OH play an important role in the reaction, especially in defluorination. When *p*-BQ was added, a slight decrease by 1.19 % and 25.37 % was observed in 4-FA degradation and defluorination efficiency, respectively. After ·OH and ·Cl were quenched, the 4-FA degradation and defluorination rates decreased by 2.98 % and 17.91 %, respectively. This is similar to the reaction data after adding IPA, indicating that ·Cl play a relatively small role in PEC process. From the result, it is observed that h^+ is the primary oxidizing species in the degradation of 4-FA. It may be due to that h^+ was generated on the valance band due to the photocatalysis, while O_2^- and ·OH were produced after a subsequent reaction. In addition, these active species have a greater impact on the defluorination rate compared to degradation rate, indicating that O_2^-, ·OH and ·Cl mainly acted on intermediate products.

3.4.2. PEC mechanism

The degradation intermediates and F^- concentration during the PEC reaction were analyzed by the GC-MS method and fluoride ion-selective electrode method, respectively. Table S2 shows that the degradation of 4-FA was a stepwise process, in which 2,4-di-*t*-butylphenol was detected as an intermediate product. The F^- concentration in the reaction solution gradually increased with the extension of reaction time, proving that the C-F bonds were effectively cleaved (Fig. S5). It indicates that the degradation mechanism of 4-FA was mainly due to the oxidation of -NH_2 and C-F by active species.

The mechanism for PEC reaction is shown in Fig. 15 based on the above results and previous reports [56,57]. The PEC system includes both electrocatalysis and photocatalysis. The electrocatalysis process mainly included direct oxidation and indirect oxidation (Eqs. (5) and (6)). When the photocatalyst (rGO/BiOI) was irradiated with a photon energy greater than the bandgap ($h\nu > E_g$), negatively charged excitation electrons transited from the valence band (VB) to the conduction band (CB), and positively charged holes were left behind in the VB. Thus, electron-hole pairs (e^-/h^+) are formed (Eq. (7)). These photogenerated carriers can also oxidize O_2 and H_2O to generate various highly reactive radicals (Eqs. (8) and (9)).

$$H_2O - e^- \rightarrow \cdot OH + H^+ \tag{5}$$

$$e^- + O_2 + H^+ \rightarrow H_2O_2 \rightarrow \cdot OH + H_2O \tag{6}$$

$$BiOI + h\nu \rightarrow BiOI\left(h_{VB}^+\right) + BiOI\left(e_{CB}^-\right) \tag{7}$$

$$BiOI\left(h_{VB}^+\right) + H_2O \rightarrow \cdot OH \tag{8}$$

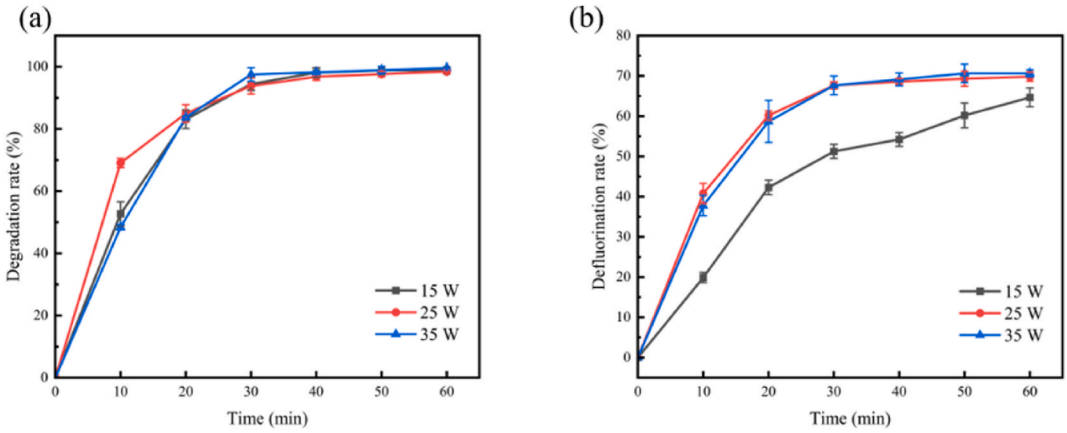

Fig. 11. 4-FA degradation (a) and defluorination (b) under different illumination strength.

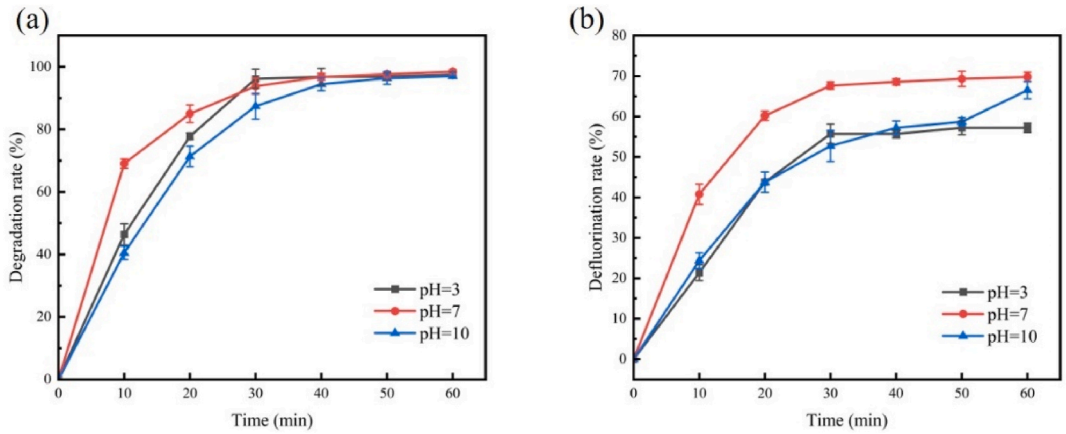

Fig. 12. 4-FA degradation (a) and defluorination (b) under different pH.

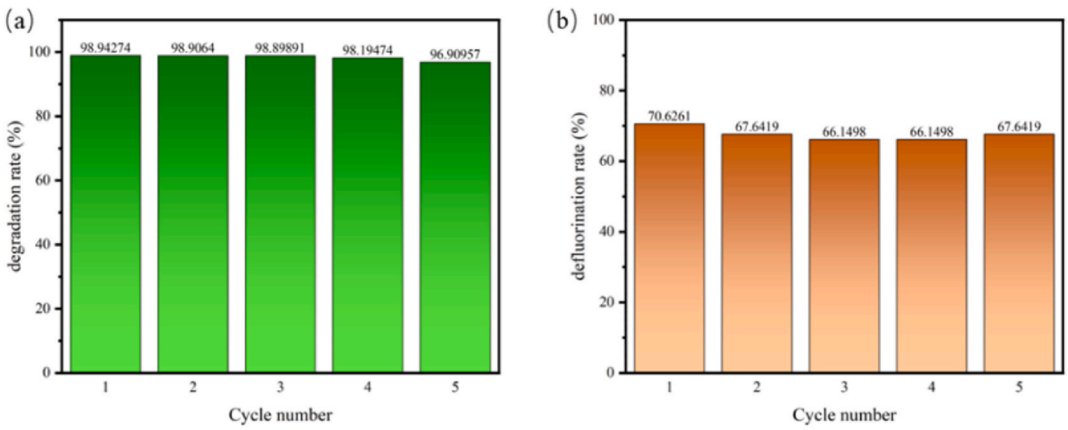

Fig. 13. Degradation rate (a) and defluorination rate (b) at different cycles.

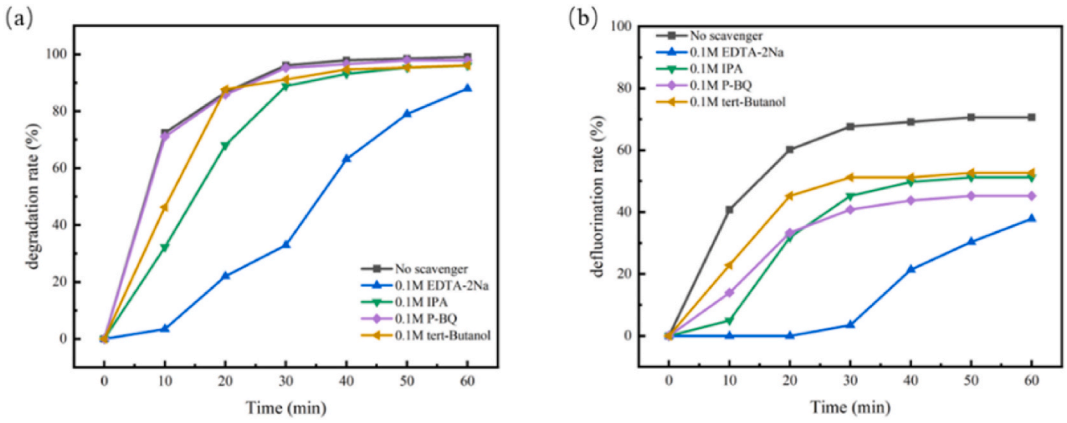

Fig. 14. The trapping experiments of reactive species of rGO/BiOI photocathode: (a) The degradation rate. (b) The defluorination rate.

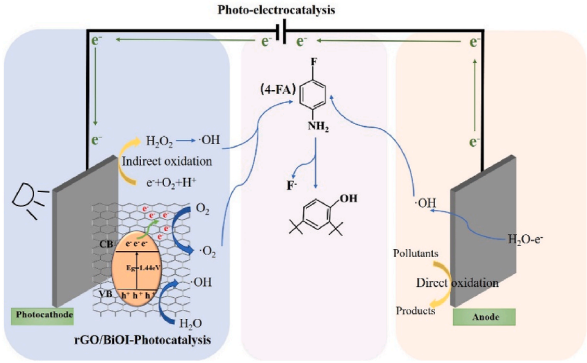

Fig. 15. The photoelectrocatalytic mechanism of rGO/BiOI-PEC process.

$$e_{CB}^{-} + O_2 \rightarrow \cdot O_2 \tag{9}$$

The CB and VB edge potentials of the photocatalyst were calculated by Eq. (10) and Eq. (11).

$$E_{VB} = X - E_C + 1/2E_g \tag{10}$$

$$E_{CB} = E_{VB} - E_g \tag{11}$$

where, *Eg* is optical bandgap (1.44 eV), E_C is energy of free electron (4.5 eV on hydrogen scale), *X* is absolute electronegativity (5.99 eV), E_{VB} is valance band edge potential, and E_{CB} is conduction band edge potential. The calculated edge potential values were 2.21 and 0.77 for VB and CB, respectively, while the calculated Fermi energy level of graphene was −0.08 V. Therefore, the photogenerated electrons could transfer from the CB of BiOI to rGO, thus reducing the electron-hole pairs recombination rate [58]. In addition, PEC can extract and transport electrons through a lower external circuit, making electrons transfer from anode to cathode and thus reducing the recombination rate of photogenerated carriers. Finally, 4-FA adsorbed on the photoelectrode surfaces, and can be degraded directly by photogenerated carriers or indirectly via reactive substances.

4. Conclusion

In summary, a rGO/BiOI photocathode was successfully proposed for highly efficient photoelectrocatalytic degradation of organic fluorine compounds in industrial sewage. The degradation and defluorination efficiency of 4-FA were 99.58 % and 72.12 %, respectively, with a NaCl concentration of 6 g/L, a current intensity of 0.75 A, an illumination strength of 15 A and a pH value of 7. Cyclic stability experiments shows that rGO/BiOI photocathode can be reused five times with only 2.03 % and 2.99 % reduction in degradation and defluorination efficiency. The main degradation product of 4-FA was 2,4-di-t-butylphenol. The PEC process had a higher performance compared to individual processes, and the design of cathode with rGO/BiOI enhance the PEC performance and stability. The findings open up a new pathway for the design of photoelectrode with stable and durable materials, and decomposition of organic fluorine compounds in the PEC system.

Data availability statement

The datasets used and analyzed during the current study available from the corresponding author on reasonable request.

CRediT authorship contribution statement

Chenhan Lv: Writing – original draft, Methodology, Data curation, Conceptualization. **Haixiang Cheng:** Writing – review & editing, Methodology, Data curation, Conceptualization. **Rui Fan:** Methodology, Formal analysis. **Jingyu Sun:** Writing – review & editing, Supervision. **Xinghai Liu:** Writing – review & editing, Project administration. **Yinghui Ji:** Validation, Investigation, Formal analysis.

Declaration of competing interest

The authors declare that they have no known competing financial interests or personal relationships that could have appeared to influence the work reported in this paper.

Acknowledgements

This work was supported by National Natural Science Foundation of China (32071626) and Competitive Science & Technology Planning Projects of Quzhou city (2020K08, 2022K32).

Appendix. ASupplementary data

Supplementary data to this article can be found online at https://doi.org/10.1016/j.heliyon.2024.e37024.

References

[1] B. Ameduri, Fluoropolymers: the right material for the right applications, Chem. Eur J. 24 (71) (2018) 18830–18841.
[2] T. Honda, I. Ojima, 8-Curious effects of fluorine on medicinally active compounds, in: K. Seppelt (Ed.), The Curious World of Fluorinated Molecules, Elsevier, 2021, pp. 241–276.
[3] B. Wang, H. Xu, D. Wang, S. He, The influence mechanism of HCO_3^- on fluoride removal by different types of aluminum salts, Colloid. Surface. A. 615 (2021) 126124.
[4] C.L. Amorim, M.F. Carvalho, C.M.M. Afonso, P.M.L. Castro, Biodegradation of fluoroanilines by the wild strain Labrys portucalensis, Int. Biodeter. Biodegr. 80 (2013) 10–15.
[5] G.E. Diwani, S.K. Amin, N.K. Attia, S.I. Hawash, Fluoride pollutants removal from industrial wastewater, Bull. Natl. Res. Cent. 46 (1) (2022) 143.
[6] K. Winkens, R. Vestergren, U. Berger, I.T. Cousins, Early life exposure to per-and polyfluoroalkyl substances (PFASs): a critical review, ECs 3 (2) (2017) 55–68.
[7] Z. Du, S. Deng, D. Liu, X. Yao, Y. Wang, X. Lu, B. Wang, J. Huang, Y. Wang, B. Xing, G. Yu, Efficient adsorption of PFOS and F53B from chrome plating wastewater and their subsequent degradation in the regeneration process, Chem. Eng. J. 290 (2016) 405–413.
[8] M. Guessous, A. Rich, S. Mountadar, M. Siniti, M. Mountadar, Treatment of an industrial wastewater for phosphorus and fluoride recovery by a process coupling block freeze concentration and precipitation, J. Cryst. Growth 619 (2023) 127335.
[9] Z. Zhao, T. Zheng, W. Zhang, X. Shen, L. Lv, M. Yan, Degradation of 3-fluoroanilne by rhizobium sp. JF-3, Biodegradation 30 (2019) 433–445.
[10] Y. Shang, X. Xu, B. Gao, S. Wang, X. Duan, Single-atom catalysis in advanced oxidation processes for environmental remediation, Chem. Soc. Rev. 50 (8) (2021) 5281–5322.
[11] Z. Du, S. Deng, Y. Bei, Q. Huang, B. Wang, J. Huang, G. Yu, Adsorption behavior and mechanism of perfluorinated compounds on various adsorbents—a review, J. Hazard Mater. 274 (2014) 443–454.
[12] N. Zhang, Y. Zhang, Y. Xu, Recent progress on graphene-based photocatalysts: current status and future perspectives, Nanoscale 4 (19) (2012) 5792–5813.
[13] M. Sansotera, F. Persico, C. Pirola, W. Navarrini, A.D. Michele, C.L. Bianchi, Decomposition of perfluorooctanoic acid photocatalyzed by titanium dioxide: chemical modification of the catalyst surface induced by fluoride ions, Appl. Catal. B Environ. 148–149 (2014) 29–35.
[14] R. Mehrkhah, S.Y. Park, J.H. Lee, S.Y. Kim, B. H Lee, Prospective performance assessment of enhanced electrochemical oxidation technology: insights into fundamentals and influencing factors for reducing energy requirements in industrial wastewater treatment, Environ. Technol. Innov. 32 (2023) 103336.
[15] C. Zhang, J. Tang, C. Peng, M. Jin, Degradation of perfluorinated compounds in wastewater treatment plant effluents by electrochemical oxidation with Nano-ZnO coated electrodes, J. Mol. Liq. 221 (2016) 1145–1150.
[16] P.A. Pullupaxi, P.J.E. Montero, C.S. Pallo, R. Vargas, L. Fernández, J.M.P. Hernández, J.L. Paz, Fundamentals and applications of photoelectrocatalysis as an efficient process to remove pollutants from water: a review, Chemosphere 281 (2021) 130821.
[17] K. Dashtian, S. Shahbazi, M. Tayebi, Z. Masoumi, A review on metal-organic frameworks photoelectrochemistry: a headlight for future applications, Coordin. Chem. Rev. 445 (2021) 214097.
[18] X. Zou, Z. Sun, Y. Hu, g-C_3N_4-based photoelectrodes for photoelectrochemical water splitting: a review, J. Mater. Chem. A. 8 (41) (2020) 21474–21502.
[19] G.C. Cabrera, P.J.E. Montero, Novel trends in mixed oxide electrodes for photoelectrocatalytic wastewater treatment, Curr. Opin. Electrochem. 44 (2024) 101448.
[20] P.F. Ibanez, S. McMichael, A.R. Cabanillas, S. Alkharabsheh, A.T. Moranchel, J. A Byrne, New trends on photoelectrocatalysis (PEC): nanomaterials, wastewater treatment and hydrogen generation, Curr. Opin. Chem. Eng. 34 (2021) 100725.
[21] Y. Guan, S. Wang, Z. Li, X. Ding, M. Wu, M. Zhang, W. Yu, Polycrystalline bismuth oxyfluoride of $BiO_{0.51}F_{1.98}$ with self-doped BiOF achieving distinctly enhanced photocatalytic activity, Mater, Lett 262 (2020) 127197.
[22] Y. Chen, L. Wang, W. Wang, M. Cao, Synthesis of Se-doped ZnO nanoplates with enhanced photoelectrochemical and photocatalytic properties, Mater. Chem. Phys. 199 (2017) 416–423.
[23] G. Li, B. Wang, J. Zhang, R. Wang, H. Liu, Rational construction of a direct Z-scheme g-C_3N_4/CdS photocatalyst with enhanced visible light photocatalytic activity and degradation of erythromycin and tetracycline, Appl. Surf. Sci. 478 (2019) 1056–1064.
[24] X. Sun, Q. Li, J. Jiang, Y. Mao, Morphology-tunable synthesis of ZnO nanoforest and its photoelectrochemical performance, Nanoscale 6 (15) (2014) 8769–8780.

[25] N.N. Rosman, R.M. Yunus, L.J. Minggu, K. Arifin, M.N.I. Salehmin, M.A. Mohamed, M.B. Kassim, Photocatalytic properties of two-dimensional graphene and layered transition-metal dichalcogenides based photocatalyst for photoelectrochemical hydrogen generation: an overview, Int. J. Hydrogen Energy 43 (41) (2018), 18925-1894.

[26] H. Zhuang, L. Lin, M. Xu, W. Xu, X. Liu, Construction of g-C3N4-based photoelectrodes towards photoelectrochemical water splitting: a review, J. Alloy. Compd. 969 (2023) 172302.

[27] N. Kumaresan, M.M.A. Sinthiya, K. Ramamurthi, R.R. Babu, K. Sethuraman, Visible light driven photocatalytic activity of ZnO/CuO nanocomposites coupled with rGO heterostructures synthesized by solid-state method for RhB dye degradation, Arab. J. Chem. 13 (2) (2020) 3910–3928.

[28] D. Huang, L. Yin, J. Niu, Photoinduced hydrodefluorination mechanisms of perfluorooctanoic acid by the SiC/graphene catalyst, Environ. Sci. Technol. 50 (11) (2016) 5857–5863.

[29] P. Kamakshi, C. Joshitha, S. Chella, S. Selvaraj, Synthesis, characterization of BiOI/rGO nanocomposite and its photocatalytic functionality analysis under visible light, Inorg. Chem. Commun. 150 (2023) 110545.

[30] M. Arumugam, S.J. Lee, T. Begildayeva, S.S. Naik, Y. Yu, H. Lee, J. Theerthagiri, M.Y. Choi, Enhanced photocatalytic activity at multidimensional interface of 1D-Bi_2S_3@2D-GO/3D-BiOI ternary nanocomposites for tetracycline degradation under visible-light, J. Hazard Mater. 404 (B) (2021) 123868.

[31] F.S. Arghavan, T.J.A. Musawi, G.A. Rumman, R. Pelalak, A. Khataee, N. Nasseh, Photocatalytic performance of a nickel ferrite/chitosan/bismuth (III) oxyiodide nanocomposite for metronidazole degradation under simulated sunlight illumination, J. Environ. Chem. Eng. 9 (4) (2021) 105619.

[32] Z. Aksu, Determination of the equilibrium, kinetic and thermodynamic parameters of the batch biosorption of nickel (II) ions onto Chlorella vulgaris, Process Biochem. 38 (1) (2002) 89–99.

[33] K. Sharma, V. Dutta, S. Sharma, P. Raizada, A.H. Bandegharaei, P. Thakur, P. Singh, Recent advances in enhanced photocatalytic activity of bismuth oxyhalides for efficient photocatalysis of organic pollutants in water: a review, J. Ind. Eng. Chem. 78 (2019) 1–20.

[34] P. Sengunthar, S. Patel, N. Thankachen, U.S. Joshi, Core–shell hybrid structured rGO decorated ZnO nanorods synthesized via a facile chemical route with photosensitive properties, New J. Chem. 45 (40) (2021) 1369–9261.

[35] N. Premalatha, L.R. Miranda, A magnetic separable 3D hierarchical BiOI/rGO/Fe_3O_4 catalyst for degradation of Rhodamine B under visible light: kinetic studies and mechanism of degradation, Mater. Sci. Eng. B-adv. 276 (2022) 115576.

[36] C. Chen, S. Chang, J. Shaya, F. Liu, Y. Lin, L. Wang, H. Tsai, C. Lu, Hydrothermal synthesis of BiOxBry/BiOmIn/GO composites with visible-light photocatalytic activity, J. Taiwan Inst. Chem. E. 133 (2022) 104272.

[37] J. Li, Q. Zhou, F. Yang, L. Wu, W. Li, R. Ren, Y. Lv, Uniform flower-like BiOBr/BiOI prepared by a new method: visible-light photocatalytic degradation, influencing factors and degradation mechanism, New J. Chem. 43 (37) (2019) 14829–14840.

[38] J. Li, F. Yang, Q. Zhou, L. Wu, W. Li, R. Ren, Y. Lv, Visible-light photocatalytic performance, recovery and degradation mechanism of ternary magnetic Fe_3O_4/BiOBr/BiOI composite, Rsc. Adv. 9 (41) (2019) 23545–23553.

[39] Y. Zhang, L. Zheng, J. Jia, K. Li, T. Zhang, H. Yu, Construction of 2D-coal-based graphene/2D-bismuth vanadate compound for effective photocatalytic CO_2 reduction to CH_3OH, Colloid. Surface. A. 639 (2022) 128321.

[40] C.H. Nguyen, M.L. Tran, T.T.V. Tran, R.S. Juang, Enhanced removal of various dyes from aqueous solutions by UV and simulated solar photocatalysis over TiO_2/ZnO/rGO composites, Sep. Purif. Technol. 232 (2020) 115962.

[41] S. Zarezadeh, A.H. Yangjeh, M. Mousavi, S. Ghosh, Synthesis of novel p-n-p BiOBr/ZnO/BiOI heterostructures and their efficient photocatalytic performances in removals of dye pollutants under visible light, J. Photoch. Photobio. A. 389 (2020) 112247.

[42] J. Niu, P. Dai, Q. Zhang, B. Yao, X. Yu, Microwave-assisted solvothermal synthesis of novel hierarchical BiOI/rGO composites for efficient photocatalytic degardation of organic pollutants, Appl. Surf. Sci. 430 (2018) 165–175.

[43] H. Wang, Y. Liang, L. Liu, J. Hu, P. Wu, W. Cui, Enriched photoelectrocatalytic degradation and photoelectric performance of BiOI photoelectrode by coupling rGO, Appl. Catal. B Environ. 208 (2017) 22–34.

[44] S. Sun, W. Wang, L. Zhang, Bi_2WO_6 quantum dots decorated reduced graphene oxide: improved charge separation and enhanced photoconversion efficiency, J. Phys. Chem. C 117 (18) (2013) 9113–9120.

[45] L. Yang, C. Xu, F. Wan, H. He, H. Gu, J. Xiong, Synthesis of RGO/BiOI/ZnO composites with efficient photocatalytic reduction of aqueous Cr (VI) under visible-light irradiation, Mater. Res. Bull. 112 (2019) 154–158.

[46] H. Wang, Y. Liang, L. Liu, J. Hu, P. Wu, W. Cui, Enriched photoelectrocatalytic degradation and photoelectric performance of BiOI photoelectrode by coupling rGO, Appl. Catal. B Environ. 208 (2017) 22–34.

[47] A.R. Benítez, R.L. Sánchez, A.R. Alonso, E.A. Estrada, R.C. Sierra, A.H. Ramírez, P.A. Lozada, L.C. Herrera, J.L. Rodríguez, Enhancing the specific capacitance of α-MnO2 through quenching-induced changes in the crystal phase structure, Int. J. Electrochem. Sc 19 (6) (2024) 100609.

[48] Z. Zhang, Q. Xiao, X. Du, T. Xue, Z. Yan, Z. Liu, H. Zhang, T. Qi, The fabrication of Ti_4O_7 particle composite modified PbO_2 coating electrode and its application in the electrochemical oxidation degradation of organic wastewater, J. Alloy. Compd. 897 (2022) 162742.

[49] J. Ali, L. Wang, H. Waseem, H.M.A. Sharif, R. Djellabi, C. Zhang, G. Pan, Bioelectrochemical recovery of silver from wastewater with sustainable power generation and its reuse for biofouling mitigation, J. Clean. Prod. 235 (2019) 1425–1437.

[50] Y. Zhou, Y. Lee, Y. Ren, M. Cui, J. Khim, Quantification of perfluorooctanoic acid decomposition mechanism applying negative voltage to anode during photoelectrochemical process, Chemosphere 284 (2021) 131311.

[51] T. Zhao, J. Pan, C. Mao, L. Chen, J. Li, H. Shao, G. Xu, Enhanced decomplexation of Cu-EDTA and simultaneous removal of Cu(II) by electron beam irradiation accompanied with autocatalytic fenton-like reaction: synergistic performance and mechanism, Chemosphere 313 (2023) 137445.

[52] S. Cherevko, S. Geiger, O. Kasian, N. Kulyk, J.P. Grote, A. Savan, B.R. Shrestha, S. Merzlikin, B. Breitbach, A. Ludwig, K.J.J. Mayrhofer, Oxygen and hydrogen evolution reactions on Ru, RuO_2, Ir, and IrO_2 thin film electrodes in acidic and alkaline electrolytes: a comparative study on activity and stability, Cata, Today Off. 262 (2016) 170–180.

[53] M.G. Alalm, M. Samy, S. Ookawara, T. Ohno, Immobilization of S-TiO2 on reusable aluminum plates by polysiloxane for photocatalytic degradation of 2,4-dichlorophenol in water, J. Water Process Eng. 26 (2018) 329–335.

[54] J. Li, X. Zhang, F. Raziq, J. Wang, C. Liu, Y. Liu, J. Sun, R. Yan, B. Qu, C. Qin, L. Jing, Improved photocatalytic activities of g-C_3N_4 nanosheets by effectively trapping holes with halogen-induced surface polarization and 2,4-dichlorophenol decomposition mechanism, Appl. Catal. B Environ. 218 (2017) 60–67.

[55] B. Darsinou, Z. Frontistis, M. Antonopoulou, I. Konstantinou, D. Mantzavinos, -activated persulfate oxidation of bisphenol A: kinetics, pathways and the controversial role of temperature, Chem. Eng. J. 280 (2015) 623–633.

[56] J. Zeng, R. Xu, A.A. El-Kady, B.T. Oranj, R. Ahmed, R. Valentin, X. Hu, W. Wu, D. Wang, J. Mao, H. Wu, X. Gu, P. Li, W. Xu, Z. Zhang, Nanomaterials enabled photoelectrocatalysis for removing pollutants in the environment and food, Trac-trend Anal. Chem. 166 (2023) 117187.

[57] L. Chen, B. Guan, J. Guo, Y. Chen, Z. Ma, J. Chen, S. Yao, C. Zhu, H. Dang, K. Shu, Z. Guo, C. Yi, K. Shi, Y. Li, J. Hua, Z. Huanga, Review on the preparation and performance improvement methods of bismuth photocatalyst materials, Catal. Sci. Technol. 13 (19) (2023) 5478–5529.

[58] S.C. Panchangam, C.S. Yellatur, J. Yang, S.S. Loka, A.Y.C. Lin, V. Vemula, Facile fabrication of TiO_2-graphene nanocomposites (TGNCs) for the efficient photocatalytic oxidation of perfluorooctanoic acid (PFOA), J. Environ. Chem. Eng. 6 (5) (2018) 6359–6369.